The Process of Mn(II) Incorporation into Aluminophosphate Zeotypes through High-Field ENDOR Spectroscopy and DFT Calculations

D. Arieli,*,† A. Delabie,‡ M. Groothaert,§ K. Pierloot,‡ and D. Goldfarb*,†

Department of Chemical Physics, Weizmann Institute of Science, Rehovot, Israel, 76100, and Department of Chemistry, University of Leuven, Celestijnenlaan 200F, B-3001 Heverlee-Leuven, Belgium, and Center for Surface Chemistry and Catalysis, University of Leuven, Kasteelpark Arenberg 23, B-3001 Heverlee-Leuven, Belgium

Received: March 11, 2002; In Final Form: June 12, 2002

High-field EPR and pulsed electron−nuclear double resonance (ENDOR) spectroscopies were used to investigate the formation of Mn−$AlPO_4$-11, Mn−$AlPO_4$-5, and Mn−SAPO-5. Samples recovered from reaction mixtures quenched at different times were subjected to EPR, ENDOR and X-ray diffraction (XRD) measurements, and the variations in the ^{31}P and ^{1}H hyperfine couplings, which are sensitive probes to the Mn−P interaction and the Mn(II) hydration, respectively, were followed. The intensity of the ^{1}H ENDOR signal decreased with reaction time, showing that the amount of both water ligands and solvent water in the Mn(II) vicinity decreased. A relatively large isotropic ^{31}P hyperfine coupling ($A_{iso}(^{31}P) \approx 7$ MHz), confirming the formation of Mn(II) framework sites, was found in all final products, whereas a smaller $A_{iso}(^{31}P)$, 4−5 MHz, was detected in samples quenched at early stages of the reaction. The latter was assigned to Mn(II) incorporated into a network of disordered aluminophosphate precursors. These precursors are formed prior to the detection of an XRD pattern, and are gradually transformed to the final three-dimensional crystalline structures. The changes in $A_{iso}(^{31}P)$ were attributed to transformations occurring both in the bonding topology and in the coordination sphere of Mn(II), where water ligands are gradually replaced by −O−P linkages. This interpretation was supported by the decrease in the intensity of the ^{1}H ENDOR signals, and by a series of DFT cluster model optimizations on intermediates of the form $[Mn(H_2O)x(OP(OH)_3)y]^{2+}$, where $x + y =$ 6, 5 or 4, followed by calculations of hyperfine coupling constants. Although the theoretical hyperfine values were overestimated with respect to the experimental ones, a satisfactory correlation was found between the trends within the calculated $A_{iso}(^{55}Mn,^{31}P)$, and the experimental trends observed during the molecular sieves formation.

Introduction

The isomorphous substitution of transition metal ions (TMI), such as Fe(III), Mn(II), or Co(II), into framework sites of aluminophosphate zeotypes has been proven to be a very useful way to improve the zeotype catalytic properties.[1−3] In these materials (MAPO's), synthetic questions concerning the specific mechanisms of metal incorporation into framework and extra-framework sites are still open. Hanson and co-workers[4−6] have used in situ synchrotron X-ray powder diffraction (XRD) to study the crystallization of AlPO's and MAPO's. They found, among others, that the nature of the incorporated transition metal influences the crystallization rate as well as the crystallization mechanism.

A different branch of experiments, aiming at following MAPO formation, exploits the rich spectroscopy associated with transition metals. These, in contrast to XRD, can probe local structures and ordering prior to the appearance of crystals. In a recent communication, Weckhuysen et al.[7] followed the coordination chemistry of Co(II) during the formation of Co−$AlPO_4$-5 by means of in situ electronic spectroscopy combined with Electron Paramagnetic Resonance (EPR). The formation of Ni−SAPO-34 was investigated by Inoue et al.[8] using NMR and electronic spectroscopies, as well as elemental analysis of samples, quenched at various temperatures during a temperature-programmed hydrothermal crystallization. These suggest that in the rapid crystallization method applied, an aluminophosphate framework is developed first, the silicon atoms are then gradually incorporated into the framework, and the nickel ions are falling into the tetrahedral sites at the last stage of crystallization. In situ ^{31}P and ^{27}Al NMR was applied to study the formation of AlPO,'s and the coordination state of aluminum and its evolution during the synthesis could be extracted.[9] Other NMR studies[10,11] concentrated on aqueous solutions containing starting materials for aluminophosphate formation.

While NMR techniques are very useful to characterize aluminophosphate molecular sieves, EPR spectroscopy is suited to investigate the incorporation of paramagnetic transition metals into them.[3] However, the EPR spectrum alone often cannot provide detailed structural information on the local environment of the transition metal center, particularly on its second and third coordination spheres. The missing information can be obtained by applying more sophisticated EPR techniques such as electron−nuclear-double-resonance (ENDOR) spectroscopy.[12,13] In the case of high-spin TMI, such as Mn(II) and Fe(III), ($S = {}^5/_2$), high-field EPR techniques ($\nu_0 \approx 95$ GHz) have been proven to be highly advantageous over conventional X-band experiments.[14−16] This is due to the higher sensitivity

† Department of Chemical Physics.
‡ Department of Chemistry.
§ Center for Surface Chemistry and Catalysis.

10.1021/jp020684s CCC: $22.00 © 2002 American Chemical Society
Published on Web 08/08/2002

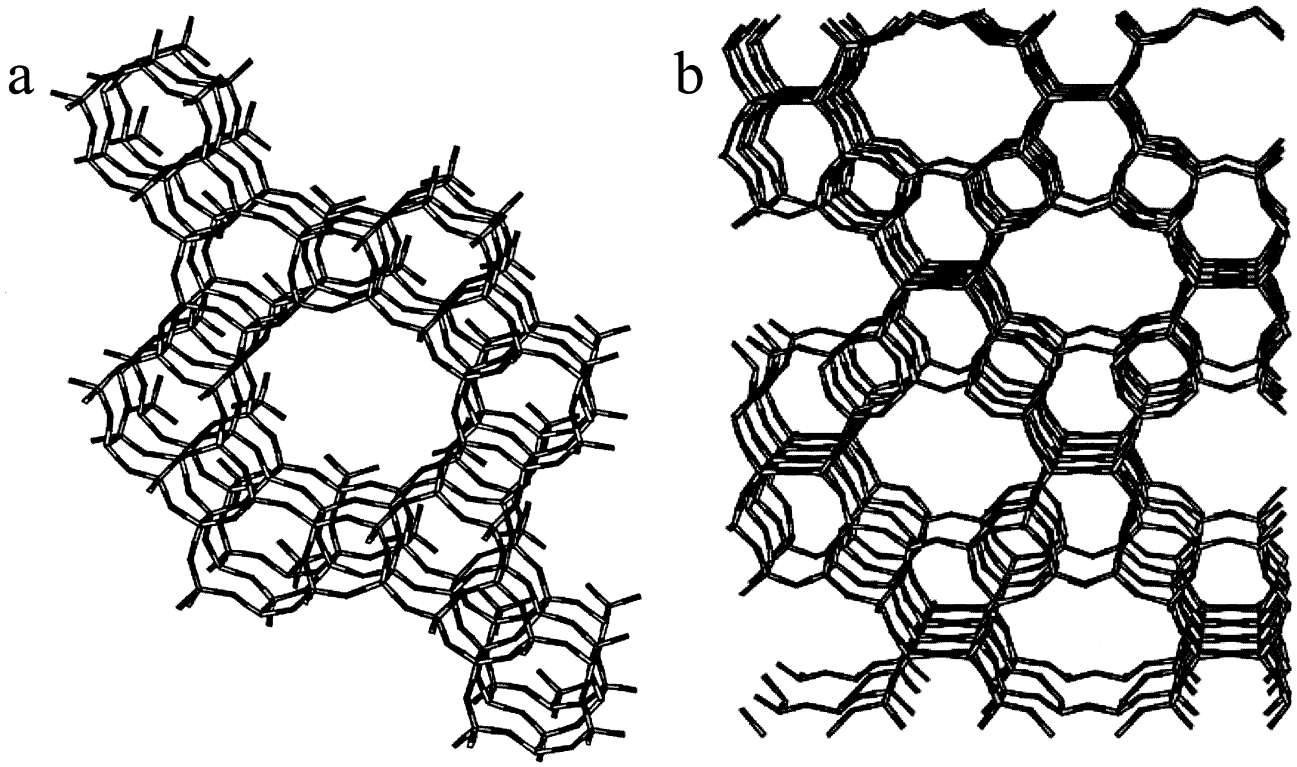

Figure 1. The structures of $AlPO_4$-5 (a) and $AlPO_4$-11 (b) zeotypes, showing a fragment containing 2 × 2 × 2 unit cells.

and thermal polarization at high fields in combination with the reduced inhomogeneous broadening caused by the zero field splitting (ZFS).[14,17] Recently developed high-field ENDOR has similarly been found most useful in the characterization of transition metals in microporous as well as mesoporous materials.[16,18] We have previously reported that the high-field ENDOR spectrum of Mn(II) incorporated into framework sites of $AlPO_4$-20 is characterized by a relatively large ^{31}P hyperfine coupling[15] ($A_{iso} \approx 8$ MHz). This is not unique to Mn−$AlPO_4$-20; in Mn−$AlPO_4$-5 and Mn−UCSB-10Mg,[19] $A_{iso}(^{31}P)$ values of 8 and 5 MHz, respectively, were reported.[20]

The implementation of density functional theory (DFT)[21,22] has also contributed to the characterization of TMI sites in zeolites. Particularly, it made it possible to perform routine geometry optimization procedures and calculate EPR parameters at a relatively low computational cost as compared to traditional ab initio techniques.[23] DFT methods have been proven to be very useful in predicting magnetic properties of transition metal complexes such as chemical shifts[24] and **g**-tensors.[25] A major complication in applying quantum chemical methods to zeolite related problems is their infinite dimension. One way to overcome this difficulty is to adopt finite models such as clusters of atoms or ions, which can be real or hypothetical molecules. This means to confine the explicit treatment to those atoms and interactions of significance for the effect under study, but to neglect or only approximately include influences of the environment. This "molecular" approach is particularly suited to tackle local phenomena,[26] e.g., to describe the active substitution sites in a modified zeolite, and it also helps to extend the knowledge on the structure and bonding of transition metal incorporated zeolites. Such an approach has been successfully used by Pierloot and co-workers[27−29] for the calculation of d−d transitions and *g*-values of Co(II) and Cu(II) ions occupying cationic positions in aluminosilicate zeolites, and recently also by Carl et al.[25] in DFT calculations of *g*-values and hyperfine coupling constants of VO^{2+} exchanged zeolites.

In this work we investigated the formation of Mn(II) framework sites during the crystallization of $AlPO_4$-11, $AlPO_4$-5, and SAPO-5[30] (see Figure 1) using high-field ENDOR spectroscopy. This method is unique in the sense that it provides direct information on the close environment of Mn(II) and the changes it undergoes during the crystallization process. Information on the formation of the Mn−O−P linkages was extracted for the first time from the evolution of the ^{31}P ENDOR spectra, whereas the changes in the Mn(II) hydration sphere was examined through the intensity of the ^{1}H ENDOR signals. The measurements were carried out on solid products obtained at various stages of the reaction. The results showed the appearance of Mn−O−P linkages well before crystals could be detected by X-ray diffraction. Furthermore, the ^{31}P isotropic hyperfine coupling was found to increases with time. This increase was attributed to changes in bonding topology, and to a gradual replacement of water ligands by −O−P− linkages. To support this interpretation we carried out DFT cluster model optimizations for intermediates of the form $[Mn(H_2O)_x(OP(OH)_3)_y]^{2+}$, where $x + y = 6$, 5, or 4, followed by hyperfine coupling constants calculations. The latter were in agreement with the experimental trends observed during the synthesis process.

Experimental and Theoretical Methods

Zeotype Synthesis. Mn−$AlPO_4$-11 and Mn−$AlPO_4$-5 were prepared using standard hydrothermal methods.[31] Mn−SAPO-5 was prepared in the form of large crystals ($c \sim 100$ μm) according to Demuth et al.[32] using the aluminum source described in a subsequent paper.[33] In a typical synthesis, manganese sulfate was dissolved in water and added to a mixture of phosphoric acid, the aluminum source and the specific template. This mixture was stirred for 30 min before the final gel was divided into several standard Teflon-lined steel autoclaves and placed in the oven. The reaction was then stopped after different times (indicated in hours on Figures 2−5) by

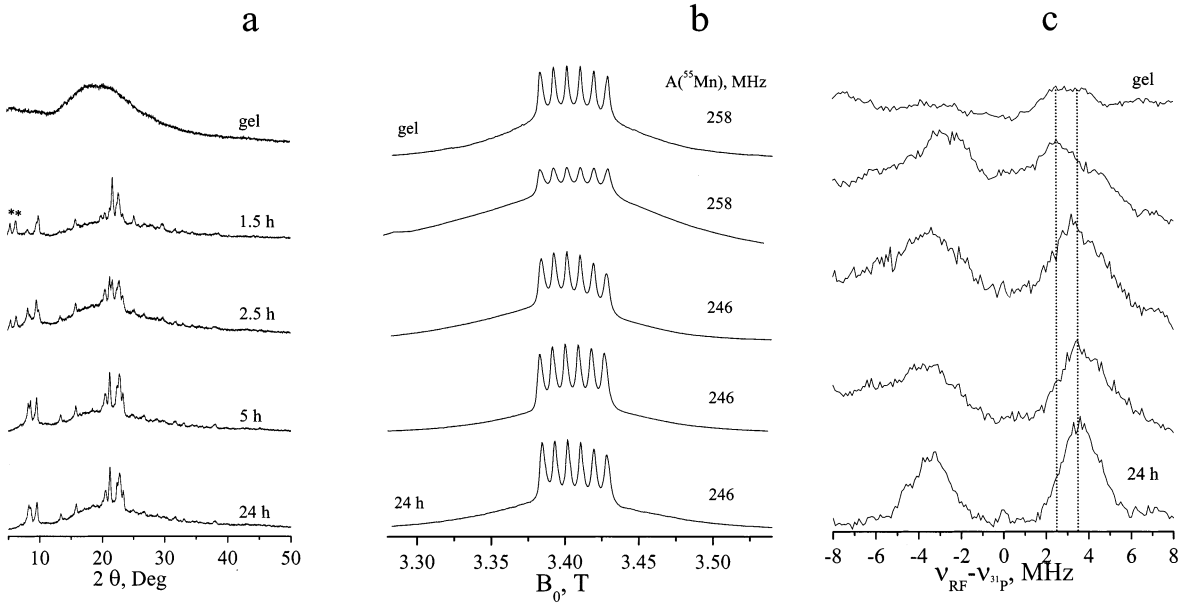

Figure 2. (a) XRD patterns, (b) FS-ED EPR spectra, and (c) ^{31}P Davies ENDOR spectra of the various samples extracted during the synthesis of Mn−$AlPO_4$-11. The dotted lines in (c) mark the shift in $A_{iso}(^{31}P)$.

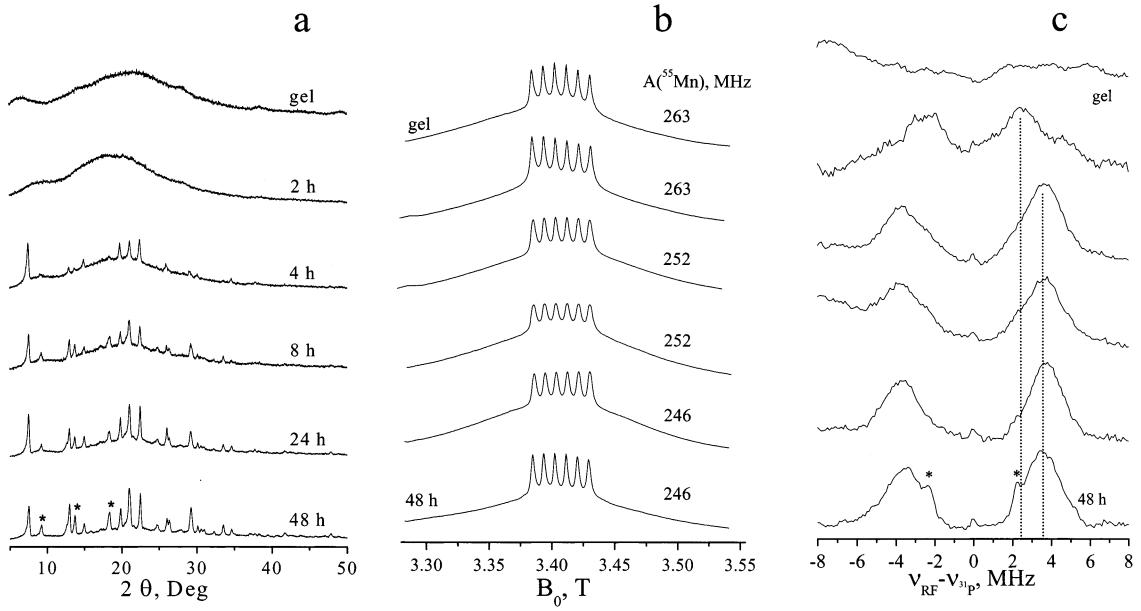

Figure 3. (a) XRD patterns, (b) FS-ED EPR spectra, and (c) ^{31}P Davies ENDOR spectra of the various samples extracted during the synthesis of Mn−$AlPO_4$-5. The dotted lines in (c) mark the shift in $A_{iso}(^{31}P)$.

ice-cooling, and the solid phase was recovered and dried overnight at 100 °C. The polycrystalline materials were recovered by centrifugation, whereas the large crystals were filtered and washed. Before introducing the samples into the EPR tubes they were exposed to air for a few hours, to allow for water saturation. ICP chemical analyses of the final product of each synthesis were as follows: Mn−$AlPO_4$-11 P/Al = 0.99, Mn/Al = 0.0009; Mn−$AlPO_4$-5 P/Al = 0.94, Mn/Al = 0.0012; Mn−SAPO-5 P/Al = 0.93, Si/Al = 0.12, Mn/Al = 0.0004. XRD measurements were carried out on a RIGAKU D diffractometer equipped with Cu *K*α radiation source, and the optical micrographs were obtained using a ZEISS optical microscope equipped with a digital camera. All samples were grounded prior to introduction into the W-band quartz tubes (0.8 mm OD).

Pulsed-EPR Measurements. W-band pulsed experiments (94.9 GHz) were carried out on a home-built spectrometer at 5 K.[34] Field swept echo detected (FS-ED) spectra were obtained using the two-pulse echo sequence with pulses of 40 and 60 ns, respectively. All ENDOR experiments were carried out at a field set to one of the ^{55}Mn hyperfine components of the $|-^1/_2, m_I\rangle \rightarrow |+^1/_2, m_I\rangle$ EPR transitions ($g \sim 2$). Davies-ENDOR spectra were obtained with microwave (MW) pulses where the π and $\pi/2$ pulse lengths were 0.2 and 0.1 μs, respectively, and a typical RF pulse length of 20 μs. Mims-ENDOR experiments were recorded with $\pi/2$ pulse duration of 0.1 μs, an RF pulse length of 20 μs, and a τ value of 0.3 μs. In the measurements performed on Mn−SAPO-5, the repetition rates were 1 and 0.5 kHz for the FS-ED EPR and ENDOR experiments, respectively. Those on Mn−$AlPO_4$-11 and Mn−$AlPO_4$-5 were carried out with rates of 0.5 and 0.2 kHz for the FS-ED EPR and ENDOR experiments, respectively. For convenience, the frequency scale in the ENDOR spectra is given relative to the corresponding Larmor frequency.

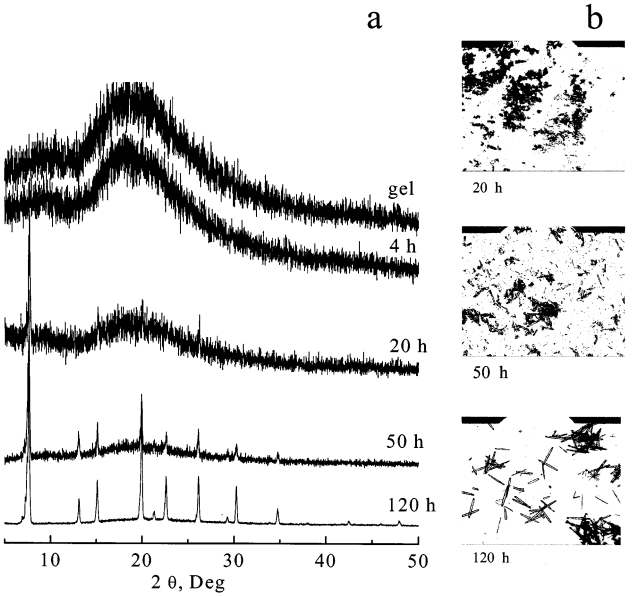

Figure 4. (a) XRD patterns and (b) optical micrographs of different samples extracted during the synthesis of Mn−SAPO-5.

Geometry Optimizations. Gas-phase full geometry optimizations were carried out by means of DFT,[21] using the Turbomole code.[35] The Becke three-parameter hybrid exchange functional[36] and the Lee−Yang−Parr[37] correlation functional, i.e., the combination commonly denoted B3LYP, were employed in all cases. This functional was proved to be very successful in previous studies of transition metal systems.[38] Basis sets from Schäfer et al.[39] were employed: For Mn a triple-ζ basis set was chosen and enhanced with two polarization functions (TZVDP), while for all other atoms triple-ζ basis sets were chosen, and enhanced with one polarization function (TZP). The following convergence criteria were used: 10^{-6} hartree for the energy change, 10^{-3} hartree/bohr for the gradients.

Hyperfine Coupling Constants Calculations. All-electron unrestricted DFT calculations of hyperfine coupling constants for different $[Mn(CN)_4]^{2-}$ geometries were done using both *Gaussian98* (G98)[40] and the Amsterdam density functional (ADF)[41] codes. The G98 calculations were done using basis sets similar to those used by Kaupp et al.[23]: for Mn a (15s11p6d)/9s7p4d basis was constructed by adding the most diffuse functions (a 1s2p1d set) from the ECP valence basis of Dolg et al.[42] to the DZ basis of Schäfer et al.[35] IGLO-III basis sets[43] were used for C and N. The tight convergence criteria (10^{-8} hartree for the energy change and 10^{-6} for the change in the density matrix) and the fine grid options (75 radial and 302 angular points) were selected for all calculations. Calculations with ADF were done at three different levels. To compare with G98, nonrelativistic calculations with DZP basis sets (designated as "III" for C, N and "II" for Mn in the ADF program) were initially performed. Two additional sets of calculations were then carried out as follows: (i) nonrelativistic calculations using TZP basis sets (designated as "IV") and (ii) scalar relativistic calculations with equivalent basis sets ("ZORA/IV"). The gradient-corrected Becke exchange[44] and Perdew correlation functional,[45] denoted as BP86 were employed in all ADF calculations. Relativistic effects were considered in the zero order relativistic approximation (ZORA).[46] The relativistic atomic potentials necessary for the relativistic calculations for each atom were calculated using the auxiliary program DIRAC, which is supplied in the ADF program package. The hyperfine calculations for the complexes of the form $[Mn(H_2O)_x(OP(OH)_3)_y]^{2+}$ were all performed using ADF at the nonrelativistic/DZP level.

Experimental Results

As pulsed EPR experiments of TMI must be carried out at cryogenic temperatures, "real" in situ spectroscopy is beyond the technical capabilities. In what follows we present the results obtained from solid samples recovered from the reaction mixture after quenching it at various stages.

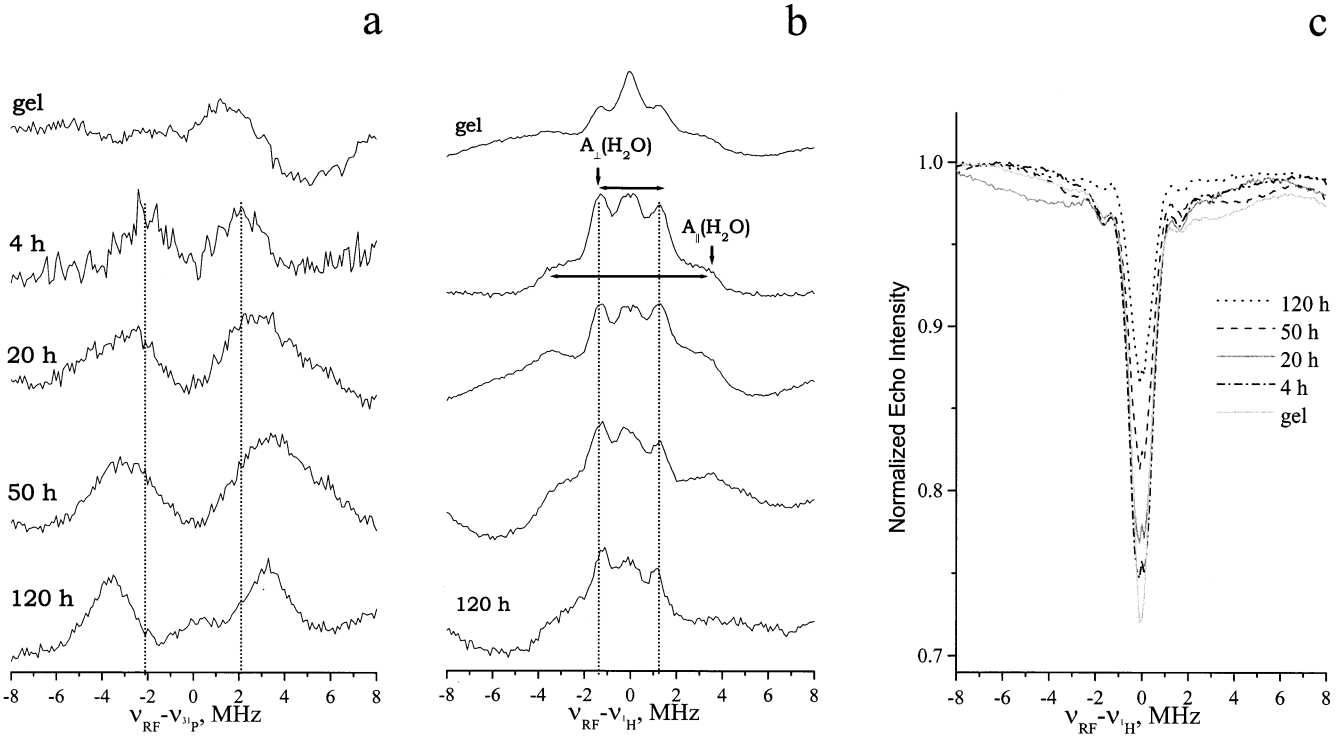

Figure 5. (a) ^{31}P Davies, (b) ^1H Davies, and (c) ^1H Mims-ENDOR spectra of the various samples extracted during the synthesis course of Mn−SAPO-5. The dotted lines in (a) and (b) mark the positions of the initial ^{31}P and ^1H doublets, respectively.

Synthesis of Mn−AlPO$_4$-11. Figure 2 presents the XRD patterns along with the normalized FS-ED EPR and ^{31}P ENDOR spectra measured during the synthesis course of Mn−AlPO$_4$-11. The relatively large background in the XRD pattern of the final product (also observed for Mn−AlPO$_4$-5) is due to technical limitations during sample preparations, and not to the presence of an amorphous material in significant amounts. Although a crystalline phase is observed already after 1.5 h of heating, the 1.5 and 2.5 h samples show two additional peaks at low 2θ angles, which are marked with asterisks on Figure 2. The latter are absent from the XRD pattern of AlPO$_4$-11,[30] observed after 5 and 24 h, and are therefore a signature for the initial formation of mixed phases. The EPR spectra show an increase in the width of each of the ^{55}Mn hyperfine components after 1.5 h, which is an indication for an increase in the distribution of the ^{55}Mn hyperfine splitting values, $A(^{55}\mathrm{Mn})$, and/or increase in the ZFS parameters during the early stages of the reaction. Then, as the synthesis progresses, this width reduces and becomes similar to that in the initial state, but with a smaller $A(^{55}\mathrm{Mn})$. Since anisotropic hyperfine components of ^{55}Mn in an octahedral or tetrahedral environment are negligibly small,[47] and cannot be determined from our experiments, we assign the splitting in the FS-ED spectra to the isotropic part, namely, $A_{iso}(^{55}\mathrm{Mn})$.

The ^{31}P ENDOR spectra of the final and intermediate products are all dominated by a broad doublet, positioned symmetrically around the ^{31}P Larmor frequency, $\nu_{^{31}\mathrm{P}}$, and characterized by a predominantly isotropic line shape. We therefore assign the splitting to the ^{31}P isotropic hyperfine coupling, $A_{iso}(^{31}\mathrm{P})$. The splitting of the various doublets are all in the range of ≈5−7 MHz, where the larger values are associated with the samples extracted at 2.5 h and onward. The change in the hyperfine splitting is also governed by a change in the breadth of each of the two hyperfine components; the line width of the final product is narrower with respect to the intermediate spectra. The asymmetry of the final doublet is attributed to baseline imperfections, as clearly inferred from the ^{31}P ENDOR spectrum of the dried gel. A prominent change in the ^{1}H ENDOR is also detected after 1.5 h of reaction, whereas later products show similar spectra, yet with lower intensity (data not shown). A complete set of ^{1}H ENDOR data is presented later for the synthesis of Mn−SAPO-5.

Synthesis of Mn−AlPO$_4$-5. To compare the syntheses of different AlPO$_4$-*n* structures, the synthesis of Mn(II) incorporated into AlPO$_4$-5 was investigated as well. In contrast to Mn−AlPO$_4$-11, the current synthesis requires 2 days for complete crystallization. Figure 3 presents the XRD patterns along with the normalized FS-ED EPR and ^{31}P ENDOR spectra of samples quenched at different times. The final product contains in addition to the AFI (AlPO$_4$-5) structure, a minor phase, indicated with asterisks in Figure 3a, which is identified as AlPO$_4$−C.[30,48] This phase has an APC topology, and has been previously observed during the synthesis of Co−AlPO$_4$-5.[49] The EPR/ENDOR spectra shown in Figures 3b,c are, in general, similar to the corresponding traces in the synthesis of Mn−AlPO$_4$-11, and exhibit the same trends (Figures 2b,c). In this synthesis a ^{31}P doublet of ≈5 MHz is observed after 2 h, before the detection of a crystalline structure in the XRD pattern. The spectrum of the final product shows a second minor doublet of ≈4.5 MHz with narrow lines (marked with asterisks in Figure 3c), which is assigned to the minor AlPO$_4$−C phase.

Synthesis of Mn−SAPO-5. The last set of measurements was carried out on Mn−SAPO-5, where silicon was introduced at a level of 15% of the aluminum content. In contrast to the first two syntheses, this material was prepared in the form of relatively large crystals ($c \sim 100\ \mu$m), following the protocol of Demuth et al.[32,33] The total time for this type of synthesis is 5 days. In addition to the XRD measurements we have also recorded the optical micrographs of the samples recovered at different stages of the reaction, and the results are shown in Figure 4 (only the last three micrographs are presented). Diffractions due to the AFI structure become clear after 20 h (Figure 4a), and turn more intense as the reaction proceeds due to the increase in the crystal size (Figure 4b).

FS-ED EPR spectra were recorded (data not shown), and the value of $A_{iso}(^{55}\mathrm{Mn})$ decreased from 260 MHz in the initial gel to 246 MHz in the final product, similar to the other two syntheses. The evolution of the ^{31}P ENDOR spectrum is displayed in Figure 5a. The ^{31}P ENDOR spectra are similar to those observed for the polycrystalline syntheses, although the initial doublet detected after 4 h is somewhat narrower and exhibits a splitting of ≈4 MHz (compare with ≈5 MHz, Figures 2c and 3c). The splitting grows and reaches ≈7 MHz after 120 h, and the line width also narrows. In this spectrum the peaks of AlPO$_4$−C are absent as the phase is pure.

Figures 5b,c present the time evolution of the Davies (b) and Mims (c) ENDOR measurements in the ^{1}H region. The latter were recorded as well, since matrix protons with small hyperfine couplings are better detected by Mims-ENDOR experiments.[34] All Mims-ENDOR spectra were normalized and are plotted superimposed on each other to allow a comparison between the various ENDOR efficiencies. The ^{1}H ENDOR data indicate a gradual decrease in the water content in the Mn(II) vicinity. The most prominent change in the Davies ENDOR spectra occurs after 4 h under hydrothermal conditions, where the relative intensity of the matrix ^{1}H signal at $\nu_{^1\mathrm{H}}$ decreases considerably, and therefore the signals at ±3.5 MHz, appear relatively more pronounced. The signal at ±3.5 MHz is attributed to $A_{||}$ of water ligands due to the $M_s = \pm 1/2$ manifold with some overlap of the $A_\perp$ feature originating from the $M_s = \pm 3/2$ manifold.[50] The spectra of the intermediate and final samples are composed of a superposition of ^{1}H signals from remaining water ligands as well as ^{1}H nuclei of the template molecules. The latter are specific organic amines which are retained in the respective zeotype cages, and contribute mainly to the signals around 1.2 MHz and below. They are most dominant in the spectrum of the final product, as manifested by a decrease from ±1.3 to ±1.2 MHz in the splitting of the inner doublet. A continuous decrease in the absolute intensity of the total ENDOR spectrum occurred throughout the course of the reaction (all measurements were done under similar accumulation conditions). Further support for the gradual change is also given by Mims ENDOR results, in which the ENDOR efficiency of the matrix line decreases as the reaction progresses.

To conclude this section we note that in all samples the ^{27}Al signal appeared only at the corresponding Larmor frequency, and there was no evidence for a substantial hyperfine coupling at any stage of the reaction.

DFT Calculations

Geometry Optimizations. The relatively large $A_{iso}(^{31}\mathrm{P})$ and the absence of a similar ^{27}Al doublet in the final product provide a direct evidence for Mn(II) framework substitution for Al, as already reported for Mn−AlPO$_4$-20.[15] To account for the changes observed in $A_{iso}(^{31}\mathrm{P},^{55}\mathrm{Mn})$ during the reaction, we carried out a series of geometry optimizations on hydrated Mn(II) clusters, where part or all water ligands are replaced by phosphoric acid moieties, and where the coordination mode of

Mn(II) is either octa-, penta- or tetrahedral. These clusters are aimed to represent local structures of Mn(II) in various intermediates generated in the reaction mixture, and the goal of the calculations performed on these clusters was to correlate the experimental changes in $A_{iso}(^{31}P,^{55}Mn)$ with changes in the Mn(II) hydration shell and coordinating ligand environment. Mn(II) is introduced into the reaction in its hydrated form: $[Mn(H_2O)_6]^{2+}$, while the phosphorus source is phosphoric acid, H_3PO_4. The reaction is conducted under acidic conditions, hence a few ionic species can generally react with $[Mn(H_2O)_6]^{2+}$. The different pK_a values of H_3PO_4 are pK_{a1} = 2.16, pK_{a2} = 7.21, and pK_{a3} = 12.32.[51] Hence, at pH ∼ 3, which is the typical pH of the initial gel,[7,52] the most abundant species are H_3PO_4 and $H_2PO_4^-$. Accordingly, we harnessed a simple model in which H_3PO_4 gradually replaces the water ligands of $[Mn(H_2O)_6]^{2+}$, where the initial process can be described as a ligand exchange reaction according to

$$[Mn(H_2O)_6]^{2+} + H_3PO_4 \rightarrow [Mn(H_2O)_5OP(OH)_3]^{2+} + H_2O \quad (1)$$

In reality, the reacting phosphate source is most probably a mixture of aluminophosphate oligomers. However, since one cannot perform geometry optimizations by means of DFT for large clusters including long aluminophosphate chains,[21,53] we substituted the latter by hydroxyls, as often done in the cluster model approach,[26,27] and focused only on the first coordination shell of Mn(II).[54] Such an approach has been proven to be successful in several recent publications, all dealing with extraframework substitution of TMI such as Cu(II), Co(II), and VO(II) in zeolites and zeotypes.[25,29] To the best of our knowledge, no applications of the cluster approach to Mn(II) framework sites in AlPO's have been reported so far. The reaction depicted in eq 1 is in agreement with an earlier NMR investigation by Mortlock et al.,[11] where the distribution of soluble aluminophosphate species in aqueous solutions containing tetramethylammonium hydroxide, phosphoric acid and aluminum chloride was characterized. There, various compositions were detected and evidences for a variety of ionic species were reported. It was concluded that in solutions of pH < 2, aluminophosphate ions are formed by the reaction of octahedral hexaaqua Al cations, $[Al{\cdot}6H_2O]^{3+}$ with H_3PO_4, $H_2PO_4^-$, and dimeric species such as $(H_3PO_4)_2$. It is reasonable to believe that many of the aluminophosphate species observed in their solution are also participating in the nucleation and crystal growth of AlPO's. The intermediates tested in our study are also consistent with the scheme proposed by Weckhuysen et al.[7] for the processes taking place during the hydrothermal crystallization of Co−$AlPO_4$-5. In that study, the formation of framework Co(II) sites was followed by in situ electronic spectroscopy.

The strategy employed in optimizing potential intermediates of the form $[Mn(H_2O)_x(OP(OH)_3)_y]^{2+}$, where $x + y = 6$, 5, or 4, was as follows: A full energy minimization was performed first on $[Mn(H_2O)_6]^{2+}$ with C_3 point group symmetry constraints.[55] Second, a full calculation was performed on $[P(OH)_4]^+$ in S_4 symmetry. The desired complex for the next optimization step was then created by interchanging optimized molecular fragments. For example, the starting geometry for $[Mn(H_2O)_5OP(OH)_3]^{2+}$ was made by replacing one of the H_2O molecules of $[Mn(H_2O)_6]^{2+}$ by a H_3PO_4 molecule, derived from $[P(OH)_4]^+$ by eliminating one of the protons.[56] More complicated molecules were created in the same manner, where each time the previously optimized fragment is utilized to create a new complex. All complexes were optimized in C_1 symmetry and are denoted hereafter as Mn−P complexes.

The complete set of gas-phase optimized structures is depicted in Figure 6. For the complexes of the form $[Mn(H_2O)_3(OP(OH)_3)_3]^{2+}$ and $[Mn(H_2O)_2(OP(OH)_3)_4]^{2+}$ two initial configurations were tested, to account for different relative positions of the ligands,[57] and both structures are shown in Figure 6d,e. This figure shows that in cases of molecules with more than one possible configuration, only a local minimum rather than a global one is obtained. Structure $\mathbf{d_I}$ is more stable by 3 kcal/mol than structure $\mathbf{d_{II}}$, while structure $\mathbf{e_I}$ is less stable than structure $\mathbf{e_{II}}$ by 5 kcal/mol. According to our model structure $\mathbf{d_I}$ is required in order to get the optimized $\mathbf{e_I}$ complex, and the same holds for structures $\mathbf{d_{II}}$−$\mathbf{e_{II}}$. Considering the error associated with DFT calculations (≳1 kcal/mol),[58] the differences in energy between each pair of optimized structures are still relatively small. Moreover, no solvent effects were taken into account in our study, as we could not perform optimizations in solution for high-spin ($S > {}^1/_2$) systems with the current Turbomole version.[59] Such effects are critical for employing thermodynamical considerations; hence, we took both structures for calculating the hyperfine structures, and made no further reference to their relative energies.

All Mn−OH_2 and Mn−$OP(OH)_3$ bond lengths of the various structures are given in Table 1. The "octahedral" configuration around Mn is conserved for all complexes containing six ligands, and for convenience we draw a dotted line between each pair of axial positions in Figure 6. The geometry of structure **g**, optimized with four ligands, is very close to a tetrahedral one.

Hyperfine Calculations. Munzarova and Kaupp[23] have recently presented a systematic study in which the hyperfine coupling constants of 21 transition metal complexes were calculated using DFT methods, employing the *Gaussian94* code. They found that, for the best cases, the isotropic hyperfine coupling constants could be determined to within 10−15%, but in other cases the differences between the experimental and calculated values were even greater. Large errors were noted especially in the calculations of ligand superhyperfine interactions. They attributed the difficulties in calculating the hyperfine coupling constants for transition metal systems to spin polarization and spin contamination effects.[60] Such effects can be particularly important for ligand nuclei, where the spin densities are 1−2 orders of magnitude smaller than those on metal nuclei.[23] Considering these findings we did not attempt to reproduce the $A_{iso}(^{31}P)$ values, but rather performed a comparative study of the optimized manganese complexes, assuming that it is possible to predict reliable trends in $A_{iso}(^{31}P)$ as a function of the geometry when employing DFT methods. Such a study can provide an insight into the mechanism of ^{55}Mn and ^{31}P coupling, and the geometrical parameters affecting the corresponding hyperfine values. We first validated the above assumption by a series of calculations performed on the tetrahedral $[Mn(CN)_4]^{2-}$ complex using both G98 and the ADF codes and different functionals. The results are presented in Appendix A.

After verifying that trends in the hyperfine values are independent of the particular level of theory, we proceeded to calculate the optimized Mn−P complexes, looking for the trends in $A_{iso}(^{31}P,^{55}Mn)$ that reproduce the experimental ones: namely, a concomitant decrease in $A_{iso}(^{55}Mn)$ and increase in $A_{iso}(^{31}P)$ in the course of the reaction. The ADF code was chosen in this case as it is more efficient than G98 for nonhybrid (pure) DFT calculations.[61] It also provides the opportunity to include relativistic effects; yet the results presented in Appendix A

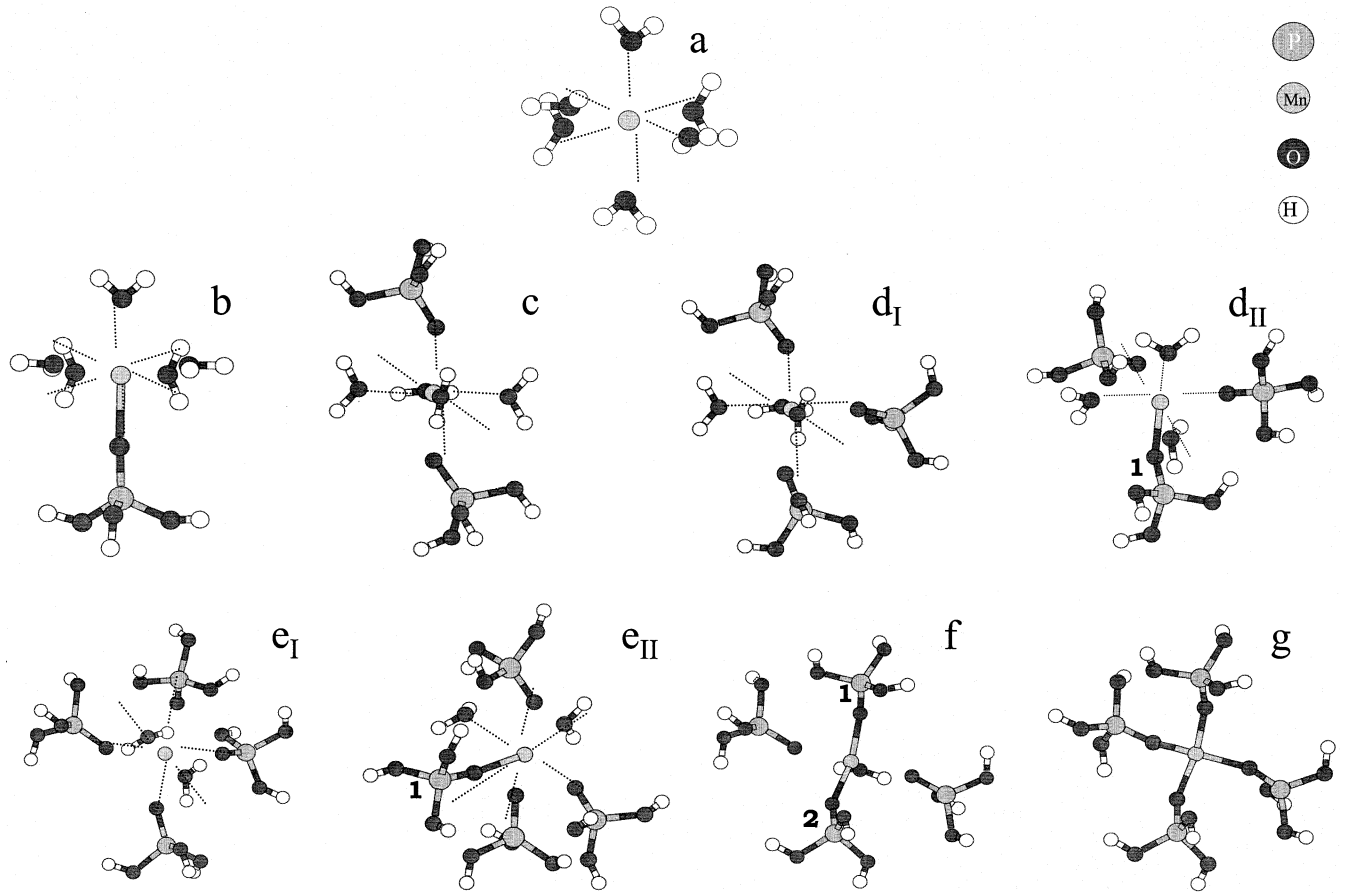

Figure 6. Optimized structures used for calculating the hyperfine values: (a) $[Mn(H_2O)_6]^{2+}$, (b) $[Mn(H_2O)_5(OP(OH)_3)]^{2+}$, (c) $[Mn(H_2O)_4(OP(OH)_3)_2]^{2+}$, (d) $[Mn(H_2O)_3(OP(OH)_3)_3]^{2+}$, (e) $[Mn(H_2O)_2(OP(OH)_3)_4]^{2+}$, (f) $[Mn(H_2O)(OP(OH)_3)_4]^{2+}$, and (g) $[Mn(OP(OH)_3)_4]^{2+}$. A dotted line is drawn between each pair of axial ligands in the hexacoordinated Mn complexes.

TABLE 1: Calculated $A_{iso}(^{55}Mn)$ (in MHz), Mn Charges (C), and Mn Spin Densities (ρ) for the Optimized $[Mn(H_2O)_x(OP(OH)_3)_y]^{2+}$ Complexes

structure	x, y	Mn−OH_2 [Å]	Mn−$OP(OH)_3$ [Å]	$A_{iso}(^{55}Mn)$	$C(^{55}Mn)^a$	$\rho(^{55}Mn)$
a	6, 0	2.22(x6)[b]		−446	1.264	4.860
b	5, 1	2.23(x2), 2.24, 2.25(x2)	2.08	−396	1.209	4.849
c	4, 2	2.23(x3), 2.25	2.15(x2)	−421	1.173	4.845
$\mathbf{d_I}$	3, 3	2.22, 2.24, 2.25,	2.16, 2.18, 2.19	−429	1.137	4.843
$\mathbf{d_{II}}$	3, 3	2.26(x3)	2.11, 2.16, 2.18	−416	1.137	4.838
$\mathbf{e_I}$	2, 4	2.24, 2.27	2.16, 2.17, 2.21(x2)	−431	1.112	4.842
$\mathbf{e_{II}}$	2, 4	2.24, 2.53	2.10, 2.13, 2.16(x2)	−394	1.098	4.831
f	1, 4	2.19	2.08, 2.09, 2.15, 2.18	−393	1.125	4.829
g	0, 4		2.05(x3), 2.06	−387	1.152	4.806

[a] Mulliken population analysis. [b] The values in parentheses represent the number of similar bonds.

demonstrate that scalar relativistic effects on high-spin Mn(II) systems are usually small, and insignificant when dealing with *trends* in the hyperfine values. Hence, we used the simplest nonrelativistic/DZP method for the Mn−P compounds. The isotropic components $A_{iso}(^{55}Mn)$ and $A_{iso}(^{31}P)$ of the calculated hyperfine tensors are given in Tables 1−2. In the case of ^{31}P the anisotropic components (T_{xx}, T_{yy}, T_{zz}) are given as well. The labels used in Figure 6 for identifying ^{31}P atoms that are relatively closer to Mn in complexes $\mathbf{d_{II}}$, $\mathbf{e_{II}}$, and **f** are indicated in the corresponding columns in parentheses. All complexes possess a double positive charge and a high spin ($S = {}^5/_2$) configuration. For further analysis the net charge, as obtained by Mulliken population analysis,[62] and the total spin densities on Mn are also presented in Table 1. These values were calculated at the same level of theory as the hyperfine values. The trends in the isotropic hyperfine values are presented in Figures 7a,b. When more than one −OP linkages occur in the same complex the averaged isotropic hyperfine coupling, $\overline{A_{iso}}$, was used to represent this complex. In cases of two different structures corresponding to the same formula, the results of the two structures were averaged as well without taking into account their energies, as discussed earlier. This averaging procedure is summed up to an error bar, which scales as the distribution in the hyperfine values.[63]

Discussion

Although the three syntheses studied differ in the time required for complete crystallization, and in some cases also in the starting materials, there are three main spectroscopic features which are common to all. First, a decrease in $A_{iso}(^{55}Mn)$ was observed during the synthesis, starting from a typical value of 260 ± 6 MHz and reaching 246 ± 6 MHz in the final crystalline products. The decrease in $A_{iso}(^{55}Mn)$ often indicates a decrease in its coordination number,[64,65] but can also arise from changes

in the type of substituents and the local geometry, namely, bond lengths and bond angles.[20] Hence, this decrease cannot unambiguously indicate whether the final coordination of Mn(II) is tetrahedral or octahedral. These results do suggest, however, that a gradual change in the Mn(II) environment takes place during the synthesis, which may be associated with decreased coordination number.

The second notable feature is the appearance of a ^{31}P doublet with $A_{iso}(^{31}P) \approx 4-5$ MHz in the initial stages of the reaction, prior to the detection of a crystalline structure in the XRD pattern. As the synthesis proceeds, the ^{31}P doublet splitting increases until a finite value of $A_{iso}(^{31}P) \approx 7$ MHz is reached. The ENDOR spectra of the final products are in agreement with earlier results obtained for Mn−$AlPO_4$-20,[15] for which $A_{iso}(^{31}P) \approx 8$ MHz was recorded. As already mentioned, the presence of a substantial ^{31}P coupling and the absence of an ^{27}Al coupling are direct evidences for framework substitution of Mn(II) for Al. The initial splitting is assigned to zeotype precursor fragments containing Mn−O−P linkages that are formed concomitantly with the aluminophosphate fragments free of Mn(II). These precursors are later transformed to the more defined three-dimensional zeotype network, which explains the change in the corresponding ENDOR line width. Although the final $A_{iso}(^{31}P)$ values are quite similar for Mn−$AlPO_4$-11 and Mn−$AlPO_4$-5, a larger variation in $A_{iso}(^{31}P)$ (5−8 MHz) was found for Mn(II) framework sites in other aluminophosphate zeotypes.[20] Large opened structures such as UCSB-6Mg and UCSB-10Mg exhibit smaller couplings compared to the denser morphologies. The sensitivity of $A_{iso}(^{31}P)$ to the structural changes is manifested, in the current study, also in the presence of an additional doublet with a splitting of 4.5 MHz due most probably to the Mn−$AlPO_4$−C impurity in Mn−$AlPO_4$-5.

The last feature is the time evolution of the ^1H signal. A continuous decrease in the amount of matrix protons is evidenced from the Mims-ENDOR spectra, while Davies-type spectra show that most of the matrix water molecules are removed at the early stage of the reaction. This is consistent with the ^{31}P ENDOR data, indicating that the Mn(II) cations are incorporated into the initial aluminophosphate network. The relatively large ^1H hyperfine couplings, appearing in the Davies spectra, are attributed to Mn(II) water ligands as well as to nearby ^1H atoms of the organic template molecules.[20,66] The decrease in the ENDOR effect of the water protons is expected since four of the water molecules in the initial $[Mn(H_2O)_6]^{2+}$ precursor must be substituted by O−P−O−(Al) moieties. As the small fragments grow up from a one-dimensional chain through a two-dimensional layer up to the final three-dimensional network, as was recently suggested by Ozin et al.,[67] the accessibility of remote water molecules to Mn(II) becomes smaller. As opposed to Inui et al.,[8] who studied the formation of Ni−SAPO-34 in a rapid crystallization method, and found that nickel ions are falling into the tetrahedral sites only at the last stage of crystallization, our study points to the very early incorporation of Mn(II) into aluminophosphate precursors, later transformed to the aluminophosphate molecular sieves.

While the correlation of the anisotropic hyperfine interaction with structural parameters such as distances is often straightforward, the quantitative interpretation of isotropic hyperfine constants in terms of bond length and bond angles requires quantum mechanical calculations. In general, the monotonic change in $A_{iso}(^{55}Mn)$ and $A_{iso}(^{31}P)$ during the formation of Mn−$AlPO_4$-11(5) can be accounted for by three mechanisms: (i) changes in the coordination sphere of Mn(II) due to ligand exchange during which water molecules are replaced by phosphoric acid derivatives (or aluminophosphate oligomers), (ii) the potential transformation of an octahedral environment into a tetrahedral one, which is governed by elimination of two water molecules, and (iii) modifications in the geometry of the initially formed Mn sites, during which Mn−O−P bond lengths and bond angles are continuously changing. We first discuss options i and ii on the bases of the calculations presented in the Results section.

The optimized structures, presented in Figure 6, all show local minimas in which the phosphoric acid moieties coordinate to Mn(II), and the initial configuration around Mn(II) (octahedral/tetrahedral, etc.) is conserved. The fact that such minimas are found suggest that related intermediates may indeed be found in the reaction mixture. As a reference we have also optimized a complex of the form $Mn(H_2O)_5(OAl(OH)_3)$, obtained by replacing one of the H_2O molecules of $[Mn(H_2O)_6]^{2+}$ by $AlO(OH)_3^{2-}$ anion, derived from $[Al(OH)_4]^-$ by eliminating one of the protons. Although the concentration of the latter is negligible at low pH, it is a very reactive (tetrahedral) species in the synthesis of aluminosilicate zeolites,[68] and therefore was selected. The optimization procedure was equivalent to that described for $[Mn(H_2O)_5(OP(OH)_3)]^{2+}$, however, as opposed to the latter, the final structure of $Mn(H_2O)_5(OAl(OH)_3)$ had significant distortions with respect to an octahedral complex (data not shown). This result serves as an indication for a preferential replacement of water ligands by phosphoric acid over the Al anion.

The calculated ^{55}Mn hyperfine interactions are almost purely isotropic, with a maximum anisotropy of 1%. The calculated $A_{iso}(^{55}Mn)$ values are about ∼50% larger than the experimental ones. The calculated ^{31}P hyperfine values have a predominant isotropic character and the absolute values are overestimated with respect to our experimental data by a factor of ∼4. Based on the DFT study of Kaupp et al.,[23] both deviations are within the "expected" range. Calculations of $A_\perp(^{31}P)$ based on the point dipole approximation[69] and the optimized r_{P-Mn} distances are shown in the right-most column of Table 2, and are also smaller than $T_{zz}/2$ by a factor of ∼3. The main source of error in the hyperfine calculations presented in this work, does not originate, in our opinion, from the cluster model but rather from limitations in the description of the hyperfine interactions in transition metal systems, where spin polarization effects become large.[23,60] Due to these large differences we chose to concentrate only on the trends observed among the various structures obtained by sequential exchange of water ligands with phosphoric acid moieties.

Figure 7a,b presents the trends in the averaged ^{55}Mn and ^{31}P hyperfine interactions within the various model clusters. The absolute values $|A_{iso}(^{55}Mn)|$ are plotted since the FS-ED EPR measurements cannot distinguish between a positive and a negative splitting. The trends obtained within the series **a**, **c**, **d**, **e**, **f**, and **g** correlate with the experimental trends for both $A_{iso}(^{55}Mn)$ and $A_{iso}(^{31}P)$. In the case of $A_{iso}(^{55}Mn)$ the variation spans a range of ∼15%, while the experimental variation amounts to ∼7% only. In the case of $A_{iso}(^{31}P)$ the change in the experimental values is 30−50%, while for the calculated values it is smaller, namely, ∼15%. These deviations imply that the change in the number/type of Mn(II) ligands cannot exclusively explain the experimental changes in the hyperfine interactions.

The size of the error bars, particularly the one corresponding to structures *d* and *e* correlates with the large experimental ^{31}P ENDOR line width, as well as the line broadening in the FS-ED spectra at the early stages of the reaction. The experimental

TABLE 2: Calculated ^{31}P Hyperfine Coupling Constants [MHz] for the Optimized Structures b−g (Figure 6) $[Mn(H_2O)_x((OP(OH)_3)_y]^{2+}$ Complexes

structure	*x*, *y*	$A_{iso}(^{31}P)$	$T_{xx}(^{31}P)$	$T_{yy}(^{31}P)$	$T_{zz}(^{31}P)$	$A_{\perp}^{a}(^{31}P)$
b	5, 1	37.6	−2.82	−2.64	5.47	0.691
c	4, 2	(1) 30.6	−2.89	−1.22	4.10	0.746
		(2) 29.5	−2.66	−1.50	4.16	0.746
d_I	3, 3	(1) 26.0	−2.47	−1.44	3.92	0.697
		(2) 29.3	−2.57	−1.48	4.05	0.703
		(3) 29.8	−2.63	−1.52	4.15	0.746
d_{II}	3, 3	(1) 38.3	−2.77	−2.53	5.30	0.733
		(2) 28.1	−2.58	−1.45	4.02	0.721
		(3) 31.6	−2.36	−1.75	4.10	0.733
e_I	2, 4	(1)27.7	−2.53	−1.40	3.92	0.733
		(2)30.7	−2.44	−1.71	4.15	0.691
		(3)27.6	−2.55	−1.37	3.91	0.691
		(4)30.6	−2.67	−1.51	4.18	0.772
e_{II}	2, 4	(1)41.5	−2.74	−2.60	5.33	0.721
		(2)28.9	−2.56	−1.78	4.34	0.607
		(3)37.1	−2.50	−2.04	4.54	0.703
		(4)30.6	−2.67	−1.51	4.18	0.772
f	1, 4	(1) 35.0	−2.45	−2.36	4.81	0.709
		(2) 37.0	−2.60	−2.34	4.95	0.733
		(3) 27.7	−2.55	−1.55	4.09	0.733
		(4) 28.1	−2.45	−1.75	4.20	0.715
g	0, 4	(1) 36.4	−2.60	−2.39	4.98	0.733
		(2) 35.5	−2.53	−2.43	4.96	0.733
		(3) 35.3	−2.58	−2.33	4.91	0.740
		(4) 33.7	−2.48	−2.35	4.83	0.753

[a] Calculations using the point dipole approximation.

line narrowing in the ^{31}P ENDOR spectra toward the end of the reaction agrees with the small error bar associated with structure **g**, which has four very similar ligands. Since the experimental $A_{iso}(^{55}Mn)$ of the final products cannot unambiguously distinguish between a tetrahedral and an octahedral Mn(II), the possible presence of framework Mn(II) species represented by clusters **e** and **f** is also likely, yet, in this case we cannot explain the line narrowing of the ENDOR spectra with our model. The data points associated with complex **b**, which has only one Mn−O−P linkage, deviate from the expected trends, and are marked on the figures with dotted circles. Another feature which does not fit the experimental findings is the small error bar associated with structure **c**. These lead us to suggest that structures related to clusters **b** and **c** cannot be detected in our experiments as they appear at very early stages of the reaction and possess relatively short lifetimes.

We now turn to discuss option (iii) based on recent DFT calculations of $A_{iso}(^{31}P,^{55}Mn)$ on a series of tetrahedral and octahedral Mn(II) complexes, $([Mn(OP(OH)_3)_4]^{2+}$ and $[Mn(OP(OH)_3)_4(H_2O)_2]^{2+}$, respectively), where the effects of the Mn−O bond length and Mn−O−P bond angles were explored.[20] There, it was found that $A_{iso}(^{31}P)$ decreases by a factor of ∼3 when the Mn−O bond length increases from 1.9 to 2.3 Å or when the Mn−O−P angle changes between 170° and 100°. The corresponding variations in $|A_{iso}(^{55}Mn)|$ were ∼10%. These results suggest that mechanism (iii) must have a significant contribution to the variation of $A_{iso}(^{31}P,^{55}Mn)$, compensating for the deficiencies of mechanisms i and ii in explaining the changes in $A_{iso}(^{31}P)$. Unfortunately, the relative contribution of each of the three mechanisms to the experimental changes in the hyperfine values cannot be fully determined from the current study. Naturally, the intermediates suggested to be present and used in the DFT calculations may all coexist at various times of the reaction and the EPR/ENDOR measurements represent some weighted average for this distribution of structures with different size, charge and geometry.

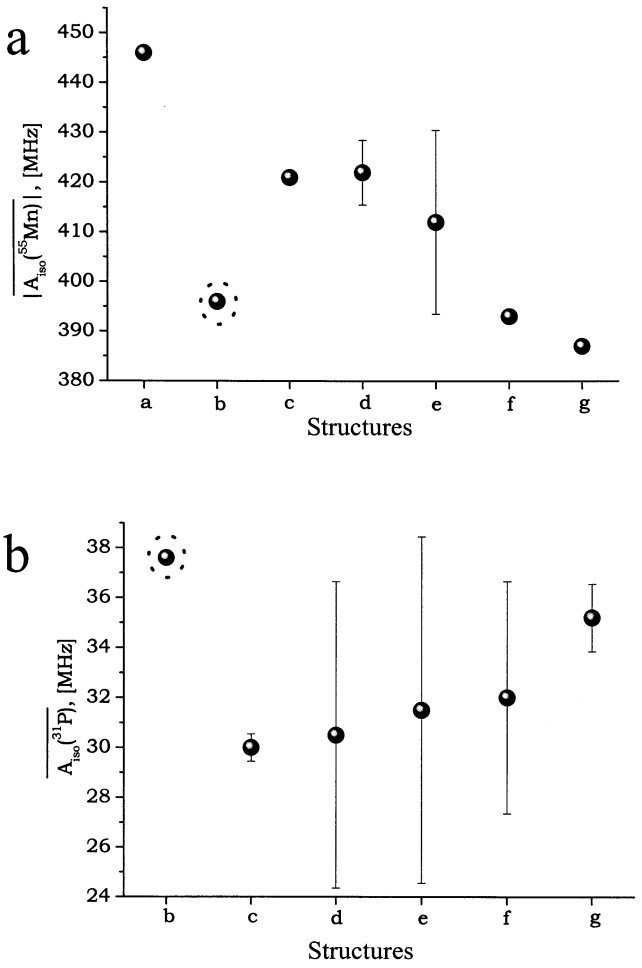

Figure 7. Calculated isotropic hyperfine coupling constants for (a) ^{55}Mn and (b) ^{31}P for the structures presented in Figure 6. The dotted circles mark the points associated with complex **b**, which deviate from the trends exhibited by the other points.

The calculated Mulliken charges and total spin densities on Mn (Table 1) imply that for an octahedral complex, replacement of water ligands by phosphoric acid reduces the charge on Mn as well as the corresponding spin density. The latter can be explained by an increase in the covalency of the Mn−O bonds and thereby a decrease in their ionic character. Once four phosphoric acid ligands are connected to Mn, the transformation from an octahedral to a tetrahedral configuration, created by water elimination, increases the charge, yet the spin density is further reduced.

Conclusion

High-field ENDOR spectroscopy allowed a direct examination of the process of Mn incorporation into the frameworks of $AlPO_4$ -n zeotypes during their synthesis through the detection of the ^{55}Mn and ^{31}P hyperfine couplings. We found that during the crystallization of Mn−$AlPO_4$-11, Mn−$AlPO_4$-5, and Mn−SAPO-5, Mn(II) is incorporated into a network of disordered aluminophosphate precursors, formed prior to the detection of an XRD pattern. These precursors are characterized by a relatively high hydration number and different Mn−O−P bonding topology as compared to the final structures.

DFT calculations of $A_{iso}(^{55}Mn)$ and $A_{iso}(^{31}P)$ along with the changes in the ^{1}H ENDOR effect provided insight into the mechanisms accounting for the time evolution of the hyperfine couplings, and shed light on the process of Mn(II) incorporation

into the framework. The presence of a series of intermediates that are formed by a gradual replacement of Mn(II) water ligands by aluminophosphate oligomers, represented by phosphoric acids, was invoked. DFT was used to optimize model compounds representing potential intermediates, for which trends in the hyperfine interactions were predicted. Although the calculated hyperfine couplings were all overestimated with respect to the experimental ones, a correlation was found between the trends in the calculated $A_{iso}(^{55}Mn)$ and $A_{iso}(^{31}P)$ and the experimental trends observed during the syntheses. The range of variation in $A_{iso}(^{31}P)$ was, however, too small, indicating that variation in the geometry of precursory tetrahedral/octahedral Mn(II) sites contributes as well.

Acknowledgment. All geometry optimizations were done using the computer facilities of the Katholieke Universiteit of Leuven (KUL). H. Vansweevelt from the KUL and Prof. J. M. L. Martin from the Weizmann Institute of Science are gratefully acknowledged for their help in setting up the quantum calculations. We are indebted to Prof. B. Weckhuysen and Prof. R. Schoonheydt from the KUL for their hospitality and for many helpful discussions. Dr. G. Ihlein from Max-Planck Institut für Kohlenforschung and Dr. G. Haran from the Weizmann Institute of Science are thanked for their assistance in making the SAPO-5 crystals. This research was supported by a grant from the United States-Israel Binational Science Foundation (BSF), Jerusalem, Israel.

Appendix A

The Performance of Different Functionals for Different $[Mn(CN)_4]^{2-}$ Geometries. In this part we tested the performance of different functionals for different geometries of a given complex. We chose the tetrahedral $[Mn(CN)_4]^{2-}$ complex, which is a simple molecule containing Mn(II), and performed the calculations using G98 for four sets of coordinations. The first set is the same (optimized) geometry used by Kaupp et al.,[23] while the next three geometries differ either in the Mn−C bond length only (elongated or shrunk) or in both the symmetry and

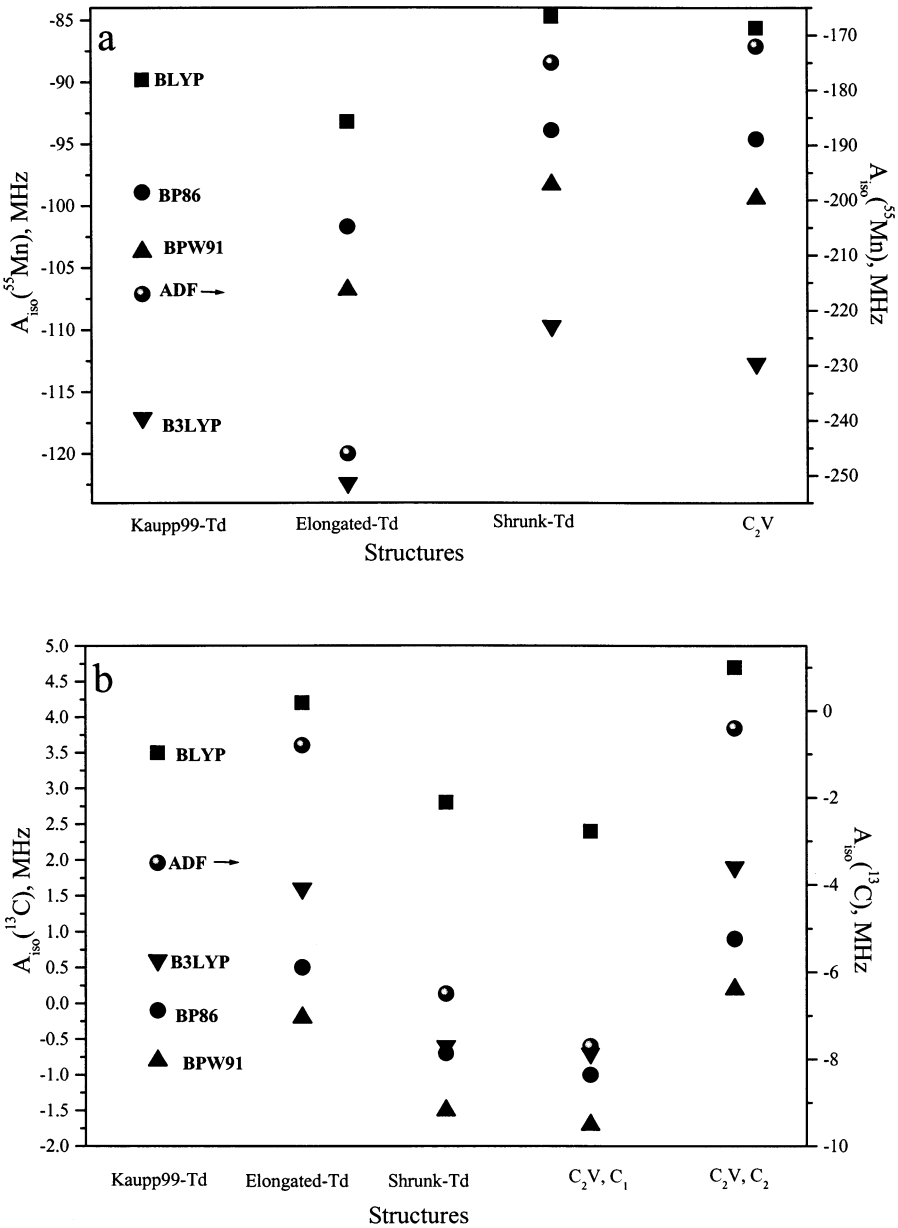

Figure A1. Calculated isotropic hyperfine coupling constants of (a) ^{55}Mn and (b) ^{13}C for four different geometries of $[Mn(CN)_4]^{2-}$. The ADF results are plotted using the right-hand scale.

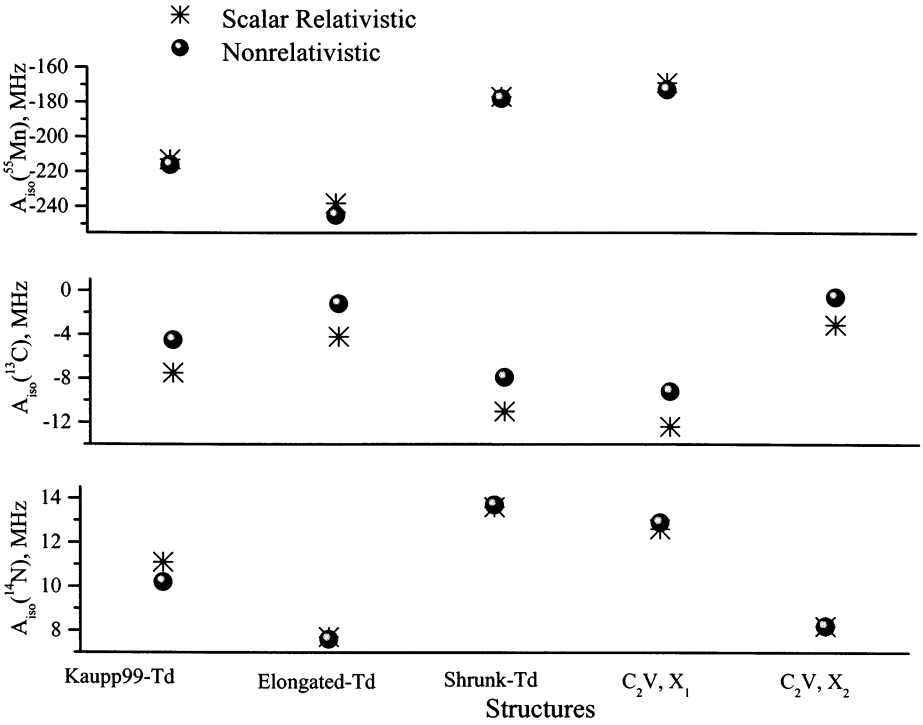

Figure A2. Isotropic hyperfine coupling constants obtained using nonrelativistic and scalar relativistic calculations for four different geometries of $[Mn(CN)_4]^{2-}$.

TABLE A1: Different Coordinate Sets Used for Calculating ^{55}Mn, ^{13}C, and ^{14}N Isotropic Hyperfine Interactions of $[Mn(CN)_4]^{2-}$

coordinates	symmetry	bond lengths, Å
Kaupp99	T_d	2.16[a] (1.13)[b]
elongated	T_d	2.26 (1.13)
shrunk	T_d	2.06 (1.13)
distorted	C_{2v}	2.16, 2.26 (1.13)

[a] Mn−C bonds. [b] C−N bonds.

the Mn−C bond length (distorted), as fully detailed in Table A1. The four following state-of-the-art exchange-correlation functionals were chosen for this examination: BLYP, BP86, BPW91, and B3LYP. The first three combine Becke gradient corrected exchange[44] with three different generalized gradient approximations for the correlation part: LYP,[37] P86,[45] and PW91.[70] The last functional employs the Becke three-parameters hybrid exchange functional[36] which includes ∼20% exact exchange. For simplification we deal only with the *isotropic* part of the full hyperfine tensor. The experimental $A_{iso}(^{55}Mn)$ of $[Mn(CN)_4]^{2-}$ in solution is −199 MHz.[23]

Relativistic Effects. The next preparatory step performed prior to the calculations on the optimized Mn−P complexes was to test the effect of scalar relativistic corrections on the trends in the hyperfine values. Similar to the above test of the selected functional, we performed a set of calculations using the ADF code with and without scalar relativistic (ZORA) corrections. The coordinates chosen are the same as for the G98 calculations.

A summary of the main results obtained for the three different elements with both software is presented in Figures A1 and A2. The results of testing different functionals on ^{14}N were similar to ^{13}C, and are omitted from Figure A1 for clarity. It is important to note that in the "distorted" (C_{2v}) geometry, two types of ^{13}C and ^{14}N are present, and X_1 is always the atom which is closer to ^{55}Mn. A close inspection of these figures reveals that despite the relatively large variation in the hyperfine coupling constants calculated with different methods, the *trends* in these values are highly reproduced for all functionals. The large differences (∼100%) between the results obtained with G98 and the ADF code for the same functional (BP86) are attributed to the differences in basis sets employed, as the isotropic hyperfine values are critically dependent on the basis set selection.[23] Based on these results we conclude that, in principle, it should be possible to *predict trends* in the hyperfine values that are associated with variations in bond length and bond angles for a given Mn(II) complex.

References and Notes

(1) Pyke, D. R.; Whitney, P.; Houghton, H. *Appl. Catal.* **1985**, *18*, 173.

(2) Wilson, S. T.; Flanigen, E. M. In *Zeolite Synthesis*; Occelli, M. L., Robson, H. E., Eds.; American Chemical Society Symposium Series; American Chemical Society: Washington, DC, 1989; pp 329−345.

(3) Hartmann, M.; Kevan, L. *Chem. Rev.* **1999**, *99*, 635.

(4) Christensen, A. N.; Jensen, T. R.; Norby, P.; Hanson, J. C. *Chem. Mater.* **1998**, *10*, 1688.

(5) Christensen, A. N.; Norby, P.; Hanson, J. C. *Chem. Mater.* **1998**, *20*, 349.

(6) Norby, P.; Christensen, A. N.; Hanson, J. C. *Inorg. Chem.* **1999**, *38*, 1216.

(7) Weckhuysen, B. M.; Baetens, D.; Schoonheydt, R. A. *Ang. Chem., Int. Ed.* **2001**, *39*, 34192.

(8) Inoue, M.; Dhupatemiya, P.; Phatansari, S.; Inui, T. *Microporous Mesoporous Mater.* **1999**, *28*, 19.

(9) Taulelle, F.; Haouas, M.; Geradin, C.; Estournes, C.; Loiseau, T.; Ferey, G. *Colloids Surf. A* **1999**, *158*, 299.

(10) Mortlock, R. F.; Bell, A. T.; Radke, C. J. *J. Phys. Chem.* **1993**, *97*, 767.

(11) Mortlock, R. F.; Bell, A. T.; Radke, C. J. *J. Phys. Chem.* **1993**, *97*, 775.

(12) Kurreck, H.; Kirste, B.; Lubitz, W. *Electron Nuclear Double Resonance Spectroscopy of Radicals in Solution*; VCH Publishers: New York, 1988.

(13) Gemperle, C.; Schweiger, A. *Chem. Rev.* **1991**, *91*, 1491.

(14) Bellew, B. F.; Halkides, C. J.; Gerfen, G. J.; Griffin, R. G.; Singel, D. J. *Biochemistry* **1996**, *35*, 12186.

(15) Arieli, D.; Vaughan, D. E. W.; Strohmaier, K. G.; Goldfarb, D. *J. Am. Chem. Soc.* **1999**, *121*, 6028.

(16) Zhang, J.; Goldfarb, D. *J. Am. Chem. Soc.* **2000**, *122*, 7034.

(17) Goldfarb, D.; Bernardo, M.; Thomann, H.; Poluektov, O. G.; Schmidt, J. *J. Am. Chem. Soc.* **1996**, *118*, 4665.

(18) Grommen, R.; Manikandan, P.; Yong, G.; Shane, T.; Shane, J. J.; Schoonheydt, R. A.; Weckhuysen, B. M.; Goldfarb, D. *J. Am. Chem. Soc.* **2000**, *122*, 11488.

(19) Bu, X.; Feng, P.; Stucky, G. D. *Science* **1997**, *278*, 2080.

(20) Arieli, D.; Delabie, A.; Strohmaier, K. G.; Vaughan, D. E. W.; Goldfarb, D.*J. Phys. Chem. B* **2002**, *106*, 7509.

(21) Kohn, W.; Becke, A. D.; Parr, R. G. *J. Phys. Chem.* **1996**, *100*, 12974.

(22) Koch, W.; Holthausten, M. C. *A Chemist's Guide to Density Functional Theory*; Wiley-VCH: New York, 2000.

(23) Munzarova, M.; Kaupp, M. *J. Phys. Chem. A* **1999**, *103*, 9966.

(24) Schreckenbach, G.; Ziegler, T. *Theor. Chem. Acc.* **1998**, *99*, 71.

(25) Carl, P. J.; Isley, S. L.; Larsen, S. C. *J. Phys. Chem. A.* **2001**, *105*, 4563.

(26) Kramer, G. J.; de Man, A. J. M.; van Santen, R. A. *J. Am. Chem Soc.* **1995**, *113*, 64351.

(27) Pierloot, K.; Delabie, A.; Ribbing, C.; Verberckmoes, A. A.; Schoonheydt, R. *J. Phys. Chem. B* **1998**, *102*, 10789.

(28) Delabie, A.; Pierloot, K.; Groothaert, M. H.; Weckhuysen, B. M.; Schoonheydt, R. *Microporous Mesoporous Mater.* **2000**, *37*, 209.

(29) Pierloot, K.; Delabie, A.; Groothaert, M. H.; Schoonheydt, R. *Phys. Chem. Chem. Phys.* **2001**, *11*, 2174.

(30) Treacy, M. M. J.; Higgins, J. B. *Collection of Simulated XRD Powder Patterns for Zeolites*, 4th ed.; Elsevier Science Publishing: New York, 2001.

(31) Wilson, S. T.; Lok, B. M.; Flanigen, E. M. U.S. Patent 4310440, 1982. Examples 2 and 32.

(32) Demuth, D.; Stucky, G. D.; Unger, K. K.; Schüth, F. *Microporous Mater.* **1995**, *3*, 473.

(33) Schunk, S. A.; Demuth, D. G.; Schulz-Dobrick, B.; Unger, K. K.; Schüth, F. *Microporous Mater.* **1996**, *6*, 273.

(34) Gromov, I.; Krymov, V.; Manikandan, P.; Arieli, D.; Goldfarb, D. *J. Magn. Reson.* **1999**, *139*, 8.

(35) Ahlrichs, R.; Bär, M.; Häser, M.; Horn, H.; Kölmel, C. *Chem. Phys. Lett.* **1989**, *162*, 165.

(36) Becke, A. D. *J. Chem. Phys.* **1993**, *98*, 5648.

(37) Lee, C.; Yang, W.; Parr, R. G.; *Phys. Rev. B* **1988**, *37*, 785.

(38) Ricca, A.; Bauschlicher Jr., C. W. *Theor. Chem. Acta* **1995**, *92*, 123.

(39) Schäfer, A.; Horn, H.; Ahlrichs, R. *J. Chem. Phys.* **1992**, *97*, 2571.

(40) Frisch, M. J.; Trucks, G. W.; Schlegel, H. B.; Scuseria, G. E.; Robb, M. A.; Cheeseman, J. R.; Zakrzewski, V. G.; Montgomery, J. A., Jr.; Stratmann, R. E.; Burant, J. C.; Dapprich, S.; Millam, J. M.; Daniels, A. D.; Kudin, K. N.; Strain, M. C.; Farkas, O.; Tomasi, J.; Barone, V.; Cossi, M.; Cammi, R.; Mennucci, B.; Pomelli, C.; Adamo, C.; Clifford, S.; Ochterski, J.; Petersson, G. A.; Ayala, P. Y.; Cui, Q.; Morokuma, K.; Malick, D. K.; Rabuck, A. D.; Raghavachari, K.; Foresman, J. B.; Cioslowski, J.; Ortiz, J. V.; Stefanov, B. B.; Liu, G.; Liashenko, A.; Piskorz, P.; Komaromi, I.; Gomperts, R.; Martin, R. L.; Fox, D. J.; Keith, T.; Al-Laham, M. A.; Peng, C. Y.; Nanayakkara, A.; Gonzalez, C.; Challacombe, M.; Gill, P. M. W.; Johnson, B. G.; Chen, W.; Wong, M. W.; Andres, J. L.; Head-Gordon, M.; Replogle, E. S.; Pople, J. A. *Gaussian98*, revision A.7; Gaussian, Inc.: Pittsburgh, PA, 1998.

(41) ADF 2.2; Department of Theoretical Chemistry, Vrije Universiteit: Amsterdam, Baerends. Te Velde, G.; Bickelhaupt, F. M.; Baerends, E.j.; Fonseca Guerra, C.; Van Gisbergen, S. J. A.; Snijders, J. G.; Ziegler, T.; *J. Comput. Chem.* **2001**, *22*, 931.

(42) Dolg, M.; Stoll, W. H.; Preuss, H. *J. Chem. Phys.* **1987**, *86*, 866.

(43) Kutzelnigg, W.; Fleischer, U.; Schindler, M. In *NMR−Basic Principles and Progress*; Springer-Verlag: Heidelberg, 1990; Vol. 23, p 165.

(44) Becke, A. D. *Phys. Rev. A* **1988**, *38*, 3098.

(45) Perdew, J. P. *Phys. Rev. B* **1986**, *33*, 8822.

(46) van Lenthe, E.; van der Avoird, A.; Wormer, P. E. S. *J. Chem. Phys.* **1998**, *108*, 4783.

(47) Reed, G. H.; Markham, D. *Biological Magnetic Resonance*; Berliner, L. J., Reuben, J., Eds.; Plenum Press: New York, 1984;Vol. 6, p 73.

(48) Keller, E. B.; Meier, W. M.; Kirchner, R. M. *Solid State Ionics*. **1990**, *43*, 93.

(49) Weckhuysen, B. M. Private communication.

(50) Tan, X.; Bernardo, M.; Thomann, H.; Scholes, C. P. *J. Chem. Phys.* **1992**, *98*, 5147.

(51) Lide, D. R. Ed. *Handbook of Chemistry and Physics*; CRC Press: Boca Raton, 2000.

(52) Szostak, R. *Molecular Sieves Principles of Synthesis and Identification*; Van Nostrand Reinhold: New York, 1989.

(53) Jensen, F. *Introduction to Computational Chemistry*; John Wiley and Sons: New York, 1999.

(54) The applications of DFT in geometry optimization are limited in the number of atoms that can be treated, and with the resources available to us, the calculations described in this work are limited to clusters of ≈40 atoms.

(55) Andriessen, J. *Mol. Phys.* **1972**, *23*, 1103.

(56) The reason for choosing $[P(OH)_4]^+$and not directly working with H_3PO_4 is the tetrahedral configuration around P in the former, which is closer to a zeotype T site configuration.

(57) We did not attempt to include *all* possible conformations in our model. For example, in $[Mn(H_2O)_4(OP(OH)_3)_2]^{2+}$ (structure **c** in Figure 6), only the conformation in which the two phosphoric acid ligands are located in trans positions, where there is minimal steric hindrance, was optimized. In the case of $[Mn(H_2O)_3(OP(OH)_3)_3]^{2+}$, we selected only the two most distinguishable structures; the conformation in which two phosphoric acid ligands are in axial positions and the third one is in the equatorial plane (structure $\mathbf{d_I}$), and the conformation in which a C_3 symmetry axis is interconnecting each set of three equivalent ligands (structure $\mathbf{d_{II}}$). The two starting geometries of the complex of the form $[Mn(H_2O)_2(OP(OH)_4)_4]^{2+}$ were derived from the final two $[Mn(H_2O)_3(OP(OH)_3)_3]^{2+}$ optimized conformations to yield structures $\mathbf{e_I}$ and $\mathbf{e_{II}}$, respectively.

(58) The mean absolute error of B3LYP for total atomization energies is 3.1 kcal/mol [Curtiss, L. A.; Raghavachari, K.; Redfern, P. C.; Pople, J. A. *J. Chem. Phys*. **1997**, *106*, 1063]. Since an isomerization energy is a much less taxing problem than total atomization, the expected error is considerably smaller. Nevertheless, we believe that it would be unreasonable to expect better than 1 kcal/mol.

(59) We have also attempted to calculate hydration energies for the gas-phase optimized complexes using G98 and the CPCM model (Barone, V.; Cossi, M. *J. Phys. Chem. A* **1998**, *102*, 1995.). Yet, this was not possible for the complexes containing four phosphoric acid ligands, most probably due to software limitations.

(60) Munzarova, M.; Kubacek, P.; Kaupp, M. *J. Am. Chem. Soc.* **2000**, *122*, 11900.

(61) The fact that the ADF results for A_{iso} (^{55}Mn) in $[Mn(CN)_4]^-$ were in better agreement with the experimental value as compared to *Gaussian98* (Appendix A) was not an argument in this case, as we did not perform a systematic hyperfine study on different high-spin Mn(II) compounds, to verify that such an agreement is not an accidental one.

(62) Mulliken, R. S. *J. Chem. Phys.* **1955**, *23*, 1833.

(63) For complexes **d** and **e**, where two different optimized structures were calculated, an average over the 6 or 8 different ^{31}P hyperfine values, respectively, was taken. The corresponding error bars are the differences between the maximum and minimum hyperfine values within each complex.

(64) De Vos, D. E.; Weckhuysen, B. M.; Bein, T. *J. Am. Chem. Soc.* **1996**, *118*, 9615.

(65) Abragam, A.; Bleaney, B. *Electron Paramagnetic Resonance of Transition Ions*; Calderon Press: Oxford, 1970; p 440.

(66) Arieli, D.; Vaughan, D. E. W.; Strohmaier, K. G.; Thomann, H.; Bernardo, M.; Goldfarb, D. *Magn. Reson. Chem.* **1999**, *37*, S43.

(67) Oliver, S.; Kuperman, A.; Ozin, G. A. *Angew. Chem., Int. Ed.* **1998**, *37*, 46.

(68) Dyer, A. *Zeolite Molecular Sieves*; John Willey and Sons: New York, 1989; p 53.

(69) Schweiger, A.; Jeschke, G. *Principles of Pulse Electron Paramagnetic Resonance*; Oxford University Press: New York, 2001.

(70) Perdew, J. P.; Wang, Y. *Phys. Rev. B* **1992**, *45*, 13244.